Energy Storage Materials 75 (2025) 104000

Contents lists available at ScienceDirect

Energy Storage Materials

journal homepage: www.elsevier.com/locate/ensm

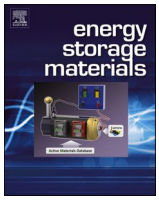

Timescale identification of electrochemical processes in all-solid-state batteries using an advanced three-electrode cell setup

Ruizhuo Zhang [a], Aleksandr Kondrakov [a,b], Jürgen Janek [a,c,*], Torsten Brezesinski [a,*]

[a] Battery and Electrochemistry Laboratory (BELLA), Institute of Nanotechnology, Karlsruhe Institute of Technology (KIT), Kaiserstr. 12, 76131 Karlsruhe, Germany
[b] BASF SE, Carl-Bosch-Str. 38, 67056 Ludwigshafen, Germany
[c] Institute of Physical Chemistry & Center for Materials Research (ZfM/LaMa), Justus-Liebig-University Giessen, Heinrich-Buff-Ring 17, 35392 Giessen, Germany

ARTICLE INFO

Keywords:
Lithium titanate
Three-electrode design
Indium-lithium alloy
Impedance
Distribution of relaxation times
Sulfide-based solid-state batteries

ABSTRACT

Two-electrode (2E) setups commonly employed in solid-state batteries (SSBs) are often not sufficient to deconvolute electrochemical processes of anode/cathode. To address this issue, herein we introduce a three-electrode (3E) cell setup, making use of an electrochemically prelithiated lithium titanate composite as reference electrode (LTO-RE). The potential/state of charge/kinetics relationship of LTO was revisited by conducting both *ex situ* and *in situ* electrochemical impedance spectroscopy measurements and corresponding distribution of relaxation times (DRT) analyses. The proposed LTO-RE maintains a stable reference potential of about 1.57 V vs. Li^+/Li with minimal drift (by 8 mV over 600 h) and negligible growth in charge-transfer resistance, enabling long-term use in 3E SSB cells. Time constants representing the involved kinetic processes are often quite close and obscure reliable assessment of contributions from different electrodes. By implementing the 3E approach, the overlap of kinetic processes between LTO working electrode and In/InLi counter electrode across a broad range of timescales can be effectively separated and identified. The proposed 3E setup offers a viable approach for thoroughly studying the interfacial kinetics of individual electrodes, thereby enhancing understanding of the underlying degradation processes in SSBs and ensuring stable long-term testing.

1. Introduction

In recent years, solid-state batteries (SSBs) or even all-solid-state batteries (ASSBs), which share a similar configuration with lithium-ion batteries (LIBs) by replacing the liquid electrolyte (LE) with a solid electrolyte (SE), have been regarded as a potential follow-up technology for the electrification process of automobiles [1]. This shift is driven by the increasing demands for safety and driving range in electric vehicles, as well as the approaching physicochemical limits of conventional LIBs [2,3]. The high ionic conductivity observed in superionic (ceramic) conductors, such as sulfide-based SEs, which can even surpass that of LEs, and the potential implementation of lithium metal anodes are paving the way for advanced SSBs to become a reality [4–6]. However, despite the promising general outlook, they still face numerous challenges. For instance, the application of sulfide-based SEs is limited by an intrinsically narrow electrochemical stability window, leading to interface-related issues, especially when coupled with layered Ni-rich oxide cathodes and/or high-capacity anodes [7,8]. Therefore, effective interface engineering of the cathode active material (CAM) and careful anode selection for electrochemical testing of SSBs at the laboratory scale are imperative [9–14].

In SSB testing, the two-electrode (2E) approach predominates due to its simplicity. Mostly, only one of the electrodes is of primary interest, often the cathode, which can then be considered as working electrode (WE) following conventional notation. Along with this, the counter electrode (CE), simultaneously used as a reference electrode (RE), is expected to provide a stable reference potential with minimal polarization. In cells with liquid electrolytes, this even leads to the rather colloquial notion of “half-cells” when a full cell with a metal anode is studied. Clearly, any conclusion on the properties of a WE in a 2E cell relies on the assumption that the CE does not contribute to the characteristics or that its own contribution can be readily subtracted. However, this assumption often fails, particularly in studies exploring the fast charging capability of the WE [15,16].

The commonly employed alloy-type CEs in SSBs, such as In/InLi, are often presumed to contribute to a minor extent to the overall overpotential and electrochemical degradation, and their effects are typically overlooked. Recent studies have highlighted the stability

* Corresponding authors.
E-mail addresses: juergen.janek@phys.chemie.uni-giessen.de (J. Janek), torsten.brezesinski@kit.edu (T. Brezesinski).

https://doi.org/10.1016/j.ensm.2025.104000
Received 13 November 2024; Received in revised form 17 December 2024; Accepted 31 December 2024
Available online 1 January 2025

limitations of the In/InLi CE and shown that microstructural deterioration at the In/InLi|SE interface during long-term cycling can lead to unexpected and substantial interfacial resistance [15,17,18]. This emphasizes the necessity of distinguishing and quantitatively analyzing the origin of degradation at the negative and positive electrodes in SSBs. Microscopic and spectroscopic techniques are capable of providing profound insights but are generally destructive. Yet, they may provide detailed information on the chemical and microstructural changes at the interface of individual electrodes, even down to the nanometer level.

In the case of sulfide-based SSBs, the cathode interface and associated degradation mechanisms have been investigated in considerable detail using various techniques, such as X-ray photoelectron spectroscopy (XPS), time-of-flight secondary ion mass spectrometry (TOF-SIMS), and transmission electron microscopy (TEM), as documented in the literature [19–22]. Electrochemical impedance spectroscopy (EIS) is widely used to monitor interfacial kinetics, as well as electrode materials under *operando* conditions in a non-destructive manner. The conventional approach of impedance analysis uses equivalent circuit model (ECM) fitting that often provides a good intuitive understanding of cell components and their behavior but relies on a number of simplifying assumptions. Problems quickly arise from the overlap of impedances with similar time constants in the frequency domain, and the different contributions from the two electrodes can hardly be separated. Therefore, it has recently become more common to first analyze the distribution of relaxation times (DRT), without assumptions on a potential equivalent circuit. Robust numerical routines are available, and DRT has meanwhile been extensively deployed in LIB research [23–26]. The transformation from frequency to time domain reveals and separates the various kinetic processes (through distinct timescales), manifested as peaks of specific shape in the DRT pattern. Any LIB relies on a number of (electro)chemical reactions, with key processes, such as interphase formation, charge transfer, or diffusion, often exhibiting similar time constants ranging from around 10^{-5} to 10^{2} s for both the WE and the CE [23]. The 3D character of real electrodes further complicates the impedance analysis, as geometric effects can lead to own impedance signals, well documented for the case of spatial constriction effects [27,28]. In general, close values of time constants and their spread may lead to misinterpretations in 2E systems.

An effective way to differentiate the contributions of individual electrodes is to employ a three-electrode (3E) measurement system, which is the standard approach in electrochemistry. This method facilitates isolation of effects from the WE and the CE by incorporating a (current-free) RE, which allows tracking the potential and impedance of the electrodes separately during electrochemical testing, provided that the RE is geometrically well defined and positioned [29]. While the implementation of 3E cell setups is widespread in LIBs [30–32], their application in SSBs remains relatively scarce [16,33–36].

Unfortunately, the development of a reliable 3E setup for SSBs faces several challenges. (i) The architecture of SSB testing setups currently lacks standardized designs, even for 2E cells. The introduction of a RE into a solid-state environment introduces rigorous manufacturing demands and spatial constraints, which are more challenging than those in liquid systems. (ii) Various materials or material combinations that can provide a constant RE potential, such as plated lithium, lithium-indium alloy, or lithium-gold alloy, along with insertion-type lithium titanate (LTO), have recently been implemented as REs in 3E cell designs for SSBs [16,29,33,36–39]. Nonetheless, some of these REs require an *in situ* lithiation step post assembly. Such a process, which typically involves connecting the RE to the WE or CE in a circuit, might initiate local volume expansion and SE decomposition near the RE, thus compromising the cell's structural integrity and potentially leading to mechanical failure. Furthermore, the thermal sensitivity of certain RE materials, e.g. lithium-gold alloy, imposes significant spatial and temporal constraints in their practical application. (iii) The integration of a RE, including its current collector (wire, mesh, or point-contact type), significantly complicates the cell design. To ensure stable testing conditions and mitigate the risk of short circuits, it is required to adopt protective measures. Overall, the logistical and technical challenges associated with constructing 3E cells far exceed those encountered in 2E setups.

Aside from that, a critical question remains whether the introduction of a RE into 3E cell setups accurately mirrors the phenomena observed in 2E cells. Regarding potential tracking, the RE size can strongly affect the outcome, due to local (geometric) blocking effects restricting ion migration [40]. For 3E EIS measurements, artifacts in the high-frequency range are often attributed to factors such as the high-impedance RE, stray capacitance from connected cables, etc. [41,42]. The shape, placement, and size of RE can also compromise the quality of impedance data, as demonstrated by computational studies [43]. It is thus important to thoroughly evaluate the comparability of 3E measurements to their 2E counterparts.

In view of these constraints, we have developed a robust 3E setup for SSB testing, delivering data that are well comparable to those collected from the corresponding 2E cells. Initially, prelithiation of an optimized LTO composite is performed electrochemically in a 2E cell (here, the LTO is considered as WE). Subsequently, the material, using a stainless steel (SS) wire as current collector, is integrated into the separator layer of a customized 3E cell as RE. Applying *ex situ* rather than *in situ* lithiation for the preparation of the LTO-RE, the reference potential can be predefined and further helps significantly enhance the structural integrity. LTO, serving as the core material in the RE, exhibits excellent chemo-mechanical properties in combination with sulfide-based SEs, which is advantageous for long-term testing in this kind of cell configuration. The LTO-RE contains the same SE employed in the separator, trying to avoid any risks associated with SE heterogeneities. Note that the latter can impede lithium transport and increase constriction resistance [35,44]. Overall, the proposed concept of RE design is facile (lack of complex processing steps), offers chemical flexibility, and can be readily implemented into practical SSB testing.

In the following, we describe all necessary steps in detail. Initially, we conducted a comprehensive investigation into the relationship between potential, state of charge (SOC), and kinetics of LTO in In/InLi|SE|LTO cells by EIS-DRT analysis and examined the stability of the LTO-RE, focusing on potential drift and charge-transfer kinetics. By constructing 3E cells in the form of In/InLi|SE|LTO-RE|SE|LTO, we observed that the DRT patterns from the different electrodes indeed overlap due to similar time constants, emphasizing the challenges in accurately distinguishing individual contributions in 2E cells. These findings underscore the necessity of using 3E configurations for enhancing the understanding of the kinetics of individual electrodes in SSBs.

2. Results and discussion

2.1. Preparation of RE and 3E cell design

Carbon-coated LTO, sourced from NEI Corp., was utilized as active material. Prior to performing any electrochemical investigations, the physical characteristics of the LTO material were assessed by X-ray diffraction (XRD), scanning electron microscopy (SEM), and energy dispersive X-ray spectroscopy (EDS), with the results provided in **Figure S1** and **Table S1** and discussed in some detail in **Supplementary Note 1**.

LTO exhibits a wide voltage plateau during (de)lithiation owing to a two-phase equilibrium involving spinel-type $Li_4Ti_5O_{12}$ and rock-salt-type $Li_7Ti_5O_{12}$ phases, making it an ideal active material for the preparation of a RE, having a stable potential of about 1.57 V vs. Li^+/Li (equivalent to 0.95 V vs. In/InLi) [38]. First, In/InLi|SE|LTO 2E cells were assembled, as shown in Fig. 1**b**, to tailor the critical parameters, including electrode composition, In/InLi CE, and most importantly, the prelithiation protocol for the LTO-RE. Aiming at minimal potential drift, the most favorable conditions identified during optimization in the 2E cells enabled the expected galvanostatic cycling, as indicated in Fig. 1**c**.

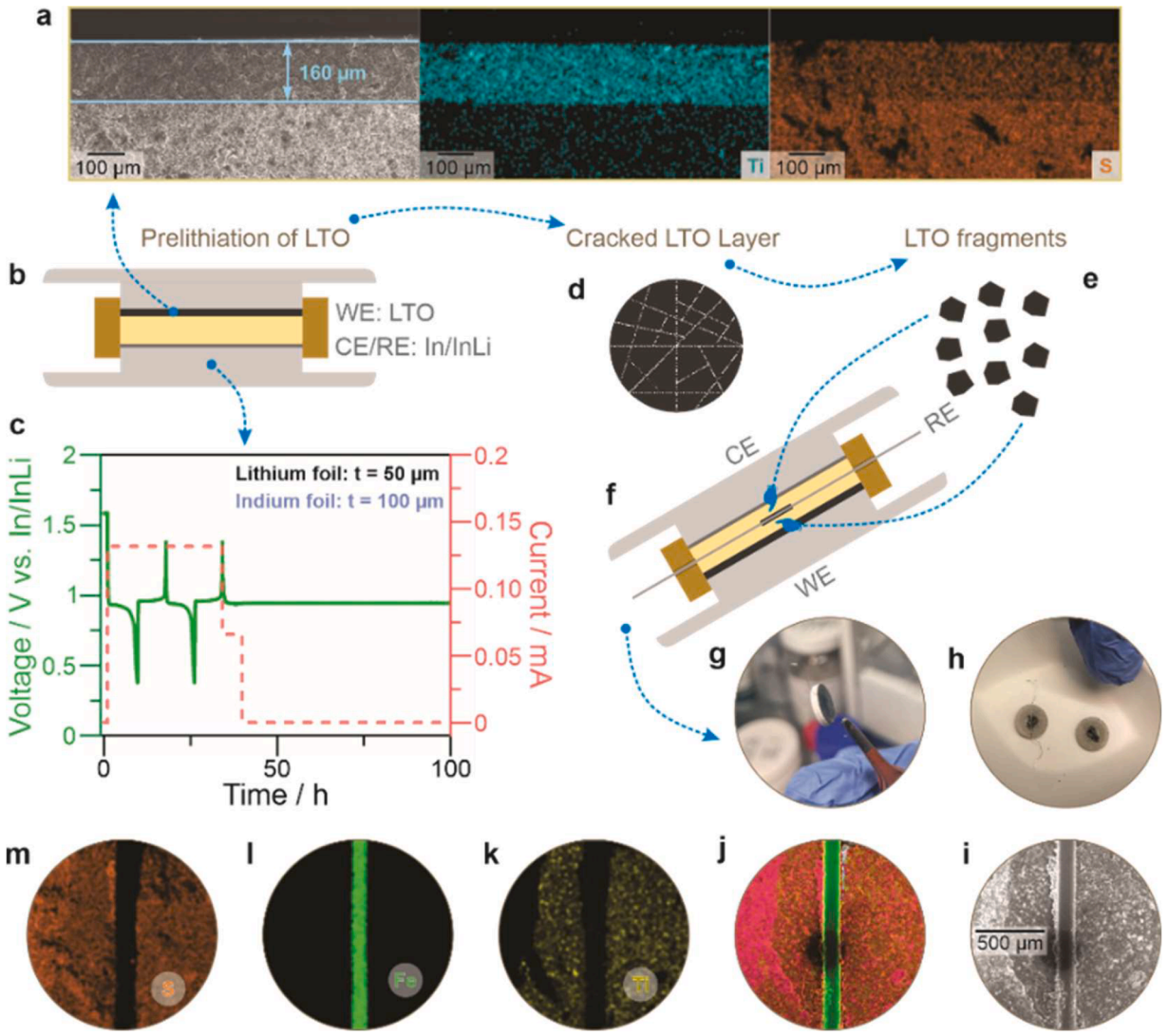

Fig. 1. Preparation of RE and design of 3E SSB cells. (a) Cross-sectional SEM image of the pelletized LTO composite and corresponding EDS mapping of Ti and S. (b) Schematic of 2E cell configuration with LTO as WE and In/InLi as CE/RE. (c) Voltage profile of an In/InLi|SE|LTO cell during prelithiation; the indium and lithium foil thicknesses are indicated. (d) Disassembled pellet after prelithiation. (e) Fragments of the prelithiated LTO composite serve as RE in 3E cells. (f) Schematic of 3E cell configuration featuring a sandwich RE design with two symmetrically embedded LTO fragments in the SE separator and an SS wire as current collector in between. (g) An assembled 3E pellet stack. (h) Inner structure of the embedded RE with corresponding (i) SEM imaging and (j–m) EDS mapping results.

The corresponding parameters are briefly listed in the following. (i) LTO composite with a weight ratio of LTO:Li_6PS_5Cl SE:Super C65 carbon black = 30:65:5 performed best and was used as WE. (ii) 100 µm thick indium foil-based In/InLi was used as CE. (iii) Initially, two formation cycles at 0.1C were performed, followed by a capacity-limited lithiation of LTO at 0.05C. 50 mAh g_{LTO}^{-1}, corresponding to a capacity of 0.375 mAh (based on the total loading of about 25 mg), was targeted to ensure LTO remains within the two-phase coexistence region during testing (see Fig. 1**c**). Interestingly, the thickness of indium foil was critical to the success of the prelithiation procedure. Using the same lithium foil of thickness 50 µm, a thicker indium foil (125 µm) led to an abnormal lithiation profile of LTO. This may be due to non-uniform alloying near the SE|In interface, resulting in hindrance of ion transport during the initial delithiation. The failure of multiple cells with the thicker indium foil is displayed in **Figure S2**.

The pelletized LTO composite layer, having a thickness of about 160 µm, was also probed using cross-sectional SEM combined with EDS mapping, as shown in Fig. 1**a**, and was then used in the RE preparation. The assembly process of 3E cells is detailed in the experimental section. As illustrated in Fig. 1**d** and **e**, after harvesting of the pellet from the 2E cell, the cracked LTO composite layer (with the SE separator attached) was further thinned, yielding individual fragments (see Fig. 1**e**). By sandwiching two pieces of LTO fragments between a thin SS wire, a symmetrically structured RE was embedded within the SE separator layer (1.47 mm thickness) of the 3E cell, as depicted in Fig. 1**f**. A practical 3E cell stack of high structural integrity is shown in Fig. 1**g**. The dissected pellet, exposing the internal structure of the LTO-RE, is displayed in Fig. 1**h**. EDS mapping performed in the vicinity of the SS wire confirmed the uniformity of the LTO-RE within the separator, as shown in Fig. 1**i**–**m**.

A critical parameter regarding the design of a 3E cell is the size of RE, which could potentially lead to ion-blocking effects [29]. To mitigate hindrance of ion transport, our design incorporates small fragments of the pelletized LTO composite and a wire-type current collector, thereby reducing size and coverage within the 3E cell. About 12.5 to 25% of the surface involved in the lithium transport pathways are covered by the embedded RE. According to the composition (see above), argyrodite Li_6PS_5Cl accounts for 65% of the as-prepared LTO-RE, while the same SE also serves as separator. This approach allows for a high degree of ion percolation through the LTO-RE. Aside from that, the *ex situ*

prelithiation of LTO (in 2E cells) ensures in advance the presence of stable interfaces between LTO and SE, thus avoiding unexpected mechanical failure near the RE, which may arise with *in situ* lithiation strategies.

LTO itself exhibits a reasonable ionic conductivity and has recently been applied in sandwich-type, multilayer SE structures for SSBs [45, 46]. Therefore, LTO and composites thereof are less likely to strongly contribute to ion blocking, unlike the current collector of RE. Considering the wire shape of the SS current collector used for the proposed RE, much lower coverage and higher robustness compared to mesh- and point contact-type counterparts can be expected.

2.2. Stability and kinetics of LTO-RE from 2E OCV-EIS analysis

Given that the LTO-RE is embedded within the SE separator throughout the duration of the 3E measurement, it is imperative to evaluate its potential drift and chemo-mechanical stability. To this end, long-term open-circuit voltage (OCV) monitoring, coupled with EIS-DRT analysis, was performed at selected time intervals on an In/InLi|SE|LTO 2E cell, as depicted in Fig. 2**a**–**d**. Prelithiated LTO (denoted as $Li_{4+x}Ti_5O_{12}$) initially displayed a potential of 0.95 V vs. In/InLi, which corresponds to 1.572 V vs. Li^+/Li [13]. A slight shift by about 8 mV toward higher potentials was observed after 600 h (selected point in time: 5), confirming the electrode's capability of sustaining a stable reference potential in a 3E setup.

As the monitoring duration extended, the OCV drift became increasingly evident, exhibiting additional increases by 11 and 46 mV over subsequent periods of 254 h (854 h) and 435 h (1035 h), respectively (selected points in time: 6 and 7). Overall, the trend in OCV drift transitioned from steady (selected points in time: 1 to 5) to accelerated increase (selected points in time: 5 to 7) throughout the monitoring period. Despite the substantial drift from the initial value, a straightforward recalibration protocol, consisting of a full discharge/charge cycle, followed by relithiation to the targeted specific capacity, was effective in correcting for this. The latter recalibration proved successful over extended measurement periods, as illustrated in **Figure S3**.

The noticeable changes in OCV suggest alterations within the electrode structure. The potential of In/InLi remains stable across a wide range of compositions, as demonstrated by coulometric titration measurements [13]. Therefore, the observed trend is more likely due to

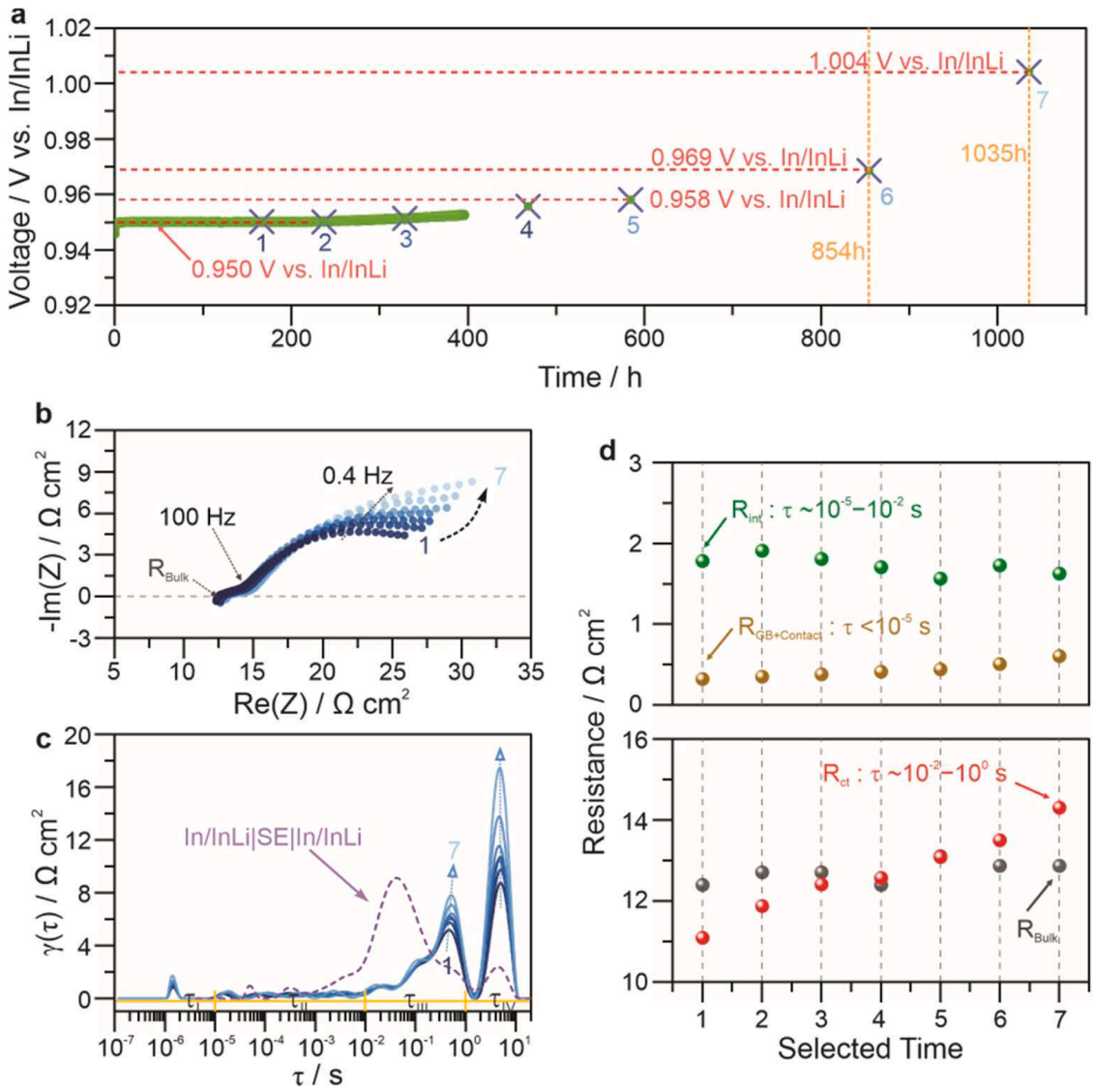

Fig. 2. OCV monitoring with EIS-DRT analysis of the In/InLi|SE|LTO cell. (a) Continuous OCV monitoring after prelithiation; selected points in time, from 1 to 7, for subsequent EIS analysis are indicated. (b) Corresponding Nyquist plots and (c) DRT patterns. The dashed purple line represents the DRT pattern of the In/InLi electrode collected from an In/InLi|SE|In/InLi symmetrical cell. (d) Fitted resistances (SE bulk, SE GB together with the contact resistance, interphase, and charge transfer) are categorized according to their characteristic time constants.

changes in the $Li_{4+x}Ti_5O_{12}$ structure, and hereafter, this discussion will refer to potential drift concerning LTO rather than OCV drift. During the period of OCV monitoring, LTO was maintained in an equilibrium state. Wagemaker *et al.* demonstrated that the lithiated LTO after relaxation exists as a solid-solution phase with nanoscale domains coexisting and exhibiting either 8*a* Li occupancy (referring to $Li_4Ti_5O_{12}$) or 16*c* Li occupancy (referring to $Li_7Ti_5O_{12}$) [47,48]. The observed potential shift may correlate with a gradual self-delithiation, from rock-salt $Li_{4+x}Ti_5O_{12}$ toward spinel $Li_4Ti_5O_{12}$, indicating a change in SOC via continuous phase transition within these nanodomains. Concurrently, because the argyrodite SE is not stable at the potential of both electrodes, slowly evolving degradation of Li_6PS_5Cl by interfacial reactions could result in microstructural changes to the LTO and/or In/InLi electrode. These would be indicated by variations in charge-transfer resistance. To elucidate the underlying kinetic processes, EIS-DRT analysis was performed.

Fig. 2**b** illustrates the evolution of impedance across the time intervals indicated in Fig. 2**a**. As can be seen, the impedance increases with prolonged monitoring, corresponding to the rising potential drift. In the EIS spectra, a barely distinguishable depressed semicircle appears in the medium- to high-frequency range (above 100 Hz), while a prominent and enlarging semicircle is apparent in the medium- to low-frequency range (below 100 Hz). To enhance visualization and quantification of the kinetic processes involved, model-independent DRT analysis was employed. This approach was supplemented by fitting individual peaks derived from the DRT patterns. An example of peak fitting is presented in **Figure S4**, while the principles of DRT are discussed in **Supplementary Note 2**, and the general procedure of data processing is depicted in **Figure S5**. Considering the different timescales of these peaks, we have categorized them into four distinct regimes based on typical kinetic processes in SSBs, as suggested in the literature [23,26].

As shown in Figs. 2**c** and **S4**, the single peak within the τ_I regime can be attributed to the grain boundary (GB) response of the Li_6PS_5Cl SE and the potential contact resistance between the electrodes and the current collector. The smaller peaks present in the slower τ_{II} regime are indicative of charge transfer across as-formed interphases, such as α-Li_2TiO_3 and In_xS_y (e.g., In_2S_3), which are principal decomposition products of LTO and In/InLi, respectively [18,49]. In the τ_{III} regime, more pronounced peaks are observed, reflecting charge-transfer processes of both electrodes. These peaks also reflect microstructural changes at the interface between the electrode active materials and the SE, demonstrating their kinetic response to SOC variations. Finally, the peak in the most sluggish kinetic regime, τ_{IV}, represents diffusive processes and additional interface-related charge-transfer processes, correlated with the respective SOC.

The evolution of the individually fitted peaks and the corresponding changes in resistance during OCV monitoring are presented in Fig. 2**c** and **d** and detailed in **Tables S2** and **S3**. The bulk resistance (R_{Bulk}) and the combined grain boundary and contact resistances ($R_{GB+Contact}$) exhibit slight increases, which may be attributed to microstructural changes either between the current collector and the electrodes or within the electrodes themselves. In contrast, the interphase resistance (R_{int}) reveals a decreasing trend, with an average value of 1.7 Ω cm^2, indicative of fast charge transport across the interphases formed at both the LTO and In/InLi electrodes. The largest changes are found for the charge-transfer resistance (R_{ct}), which increased linearly from 11.1 to 14.3 Ω cm^2.

To examine the charge-transfer characteristics of the LTO and In/InLi electrodes, a symmetric cell (In/InLi|SE|In/InLi) was fabricated and cycled galvanostatically to mimic the In/InLi|SE interface in the In/InLi|SE|LTO 2E cell. The respective Nyquist plot and DRT pattern are presented in Figs. 2**c** and **S6**. The most significant peak for In/InLi in the DRT pattern, located in the τ_{III} regime, is characterized by a time constant of $4.2{\cdot}10^{-2}$ s, in agreement with that reported in the literature [50]. This peak corresponds well with peak "P5" (see **Figure S4**) for the In/InLi|SE|LTO 2E cell, as summarized in **Table S2**. Throughout the entire OCV monitoring period (selected points in time: 1 to 7), the "P5" peak remained unaltered at about 1.1 Ω cm^2. Consequently, it can be inferred that the continuous increase in R_{ct} primarily originates from the LTO side. During OCV monitoring, microstructural changes within the electrode somewhat impede ion transport. However, the rate of increase in R_{ct} over the entire duration (1035 h) was determined to be only 0.003 Ω cm^2 h^{-1}, suggesting that this does not significantly affect charge transport during prolonged operation as RE.

The observed deviation from the flat voltage plateau suggests a gradual phase transition in $Li_{4+x}Ti_5O_{12}$, which correlates with changes in SOC. Given that the lithium diffusivity in LTO depends upon the SOC [51,52], examination of the peak in the τ_{IV} regime revealed a steady, then accelerated increase in peak intensity. This behavior aligns with the observed trend in potential drift. To further explore the relationship between potential, SOC, and kinetics in LTO, *in situ* EIS-DRT analysis was performed, as detailed in the subsequent section.

2.3. *In situ* 2E EIS-DRT analysis

By applying an ultra-low current (0.05C) for tailoring the degree of (de)lithiation, selected SOCs (labeled from 1 to 18, see Fig. 3**a**) were probed *in situ* using EIS-DRT analysis. The corresponding measured OCVs and specific capacities are given in **Table S4**. In particular, the interface-related kinetics, which is affected by variations in SOC, was examined, as illustrated in Fig. 3**b**–**g**. As the Li^+ ions are inserted/extracted into/from the LTO during discharge and charge, respectively, the composition of the lithium-indium alloy varies reversibly between $Li_{0.27}In$ (lithiated state) and $Li_{0.15}In$ (delithiated state). For details on the calculation, see **Supplementary Note 3** and **Table S5**. As expected, compared to LTO, the evolution of peaks associated with the In/InLi electrode in the DRT patterns is relatively minor [50]. Consequently, they predominantly reflect the kinetics of LTO with varying SOC. Notably, dominant peaks in the τ_{III} and τ_{IV} regimes indicate major SOC-dependent interfacial charge-transfer processes and solid-state diffusive processes within the LTO particles.

Considering the phase transitions within the nanodomains of LTO, continuous lithiation leads to a transformation from spinel $Li_4Ti_5O_{12}$ to rock-salt $Li_7Ti_5O_{12}$, progressing from SOC 1 to 9. The differences in the apparent lithium diffusion coefficient between $Li_4Ti_5O_{12}$ ($1.6{\cdot}10^{-11}$ cm^2 s^{-1}) and $Li_7Ti_5O_{12}$ ($1{\cdot}10^{-12}$ cm^2 s^{-1}) result in decreasing ion mobility with increasing rock-salt phase fraction [53]. It is also noteworthy that even minor lithium insertion into $Li_4Ti_5O_{12}$ significantly enhances the electronic conductivity, by four to six orders of magnitude [54]. Thus, the rate-limiting factor is the ionic conductivity rather than the electronic conductivity, which is more pronounced in solid-state systems. As the Li concentration within the LTO particles increases, ion mobility decreases, demonstrating its SOC-dependent nature.

High reversibility is apparent from the subsequent charging process, which involves continuous delithiation of LTO and lithiation of In/InLi, progressing from SOC 10 to 18. As $Li_7Ti_5O_{12}$ is converted back to $Li_4Ti_5O_{12}$, the increasing fraction of the latter phase enhances the overall lithium diffusivity. From SOC 10 to 16, the interface-related kinetic hindrance consistently decreases. From SOC 17 to 18, near the completion of phase transition, a resurgence of peaks in the τ_{III} and τ_{IV} regimes is observed (see **Figure S7**). This indicates emerging charge-transfer issues at the interface between LTO and SE, as well as an accompanying diffusive or phase transition-induced sluggish process within the particle's interior during the final stages of delithiation. The corresponding changes in resistances are depicted in Fig. 3**f** and **g**. The results from peak fitting and the individual resistances, classified by their characteristic time constants, are summarized in **Tables S6**–**S9**. Interestingly, the R_{bulk} remained virtually constant throughout both discharge and charge, indicating SOC independence. In contrast, the $R_{GB+Contact}$ exhibited a slight increase during charge, but maintained a constant value of 0.4 Ω cm^2 during discharge. The R_{int} and, most notably, the R_{ct} revealed a strong correlation with the SOC. During the

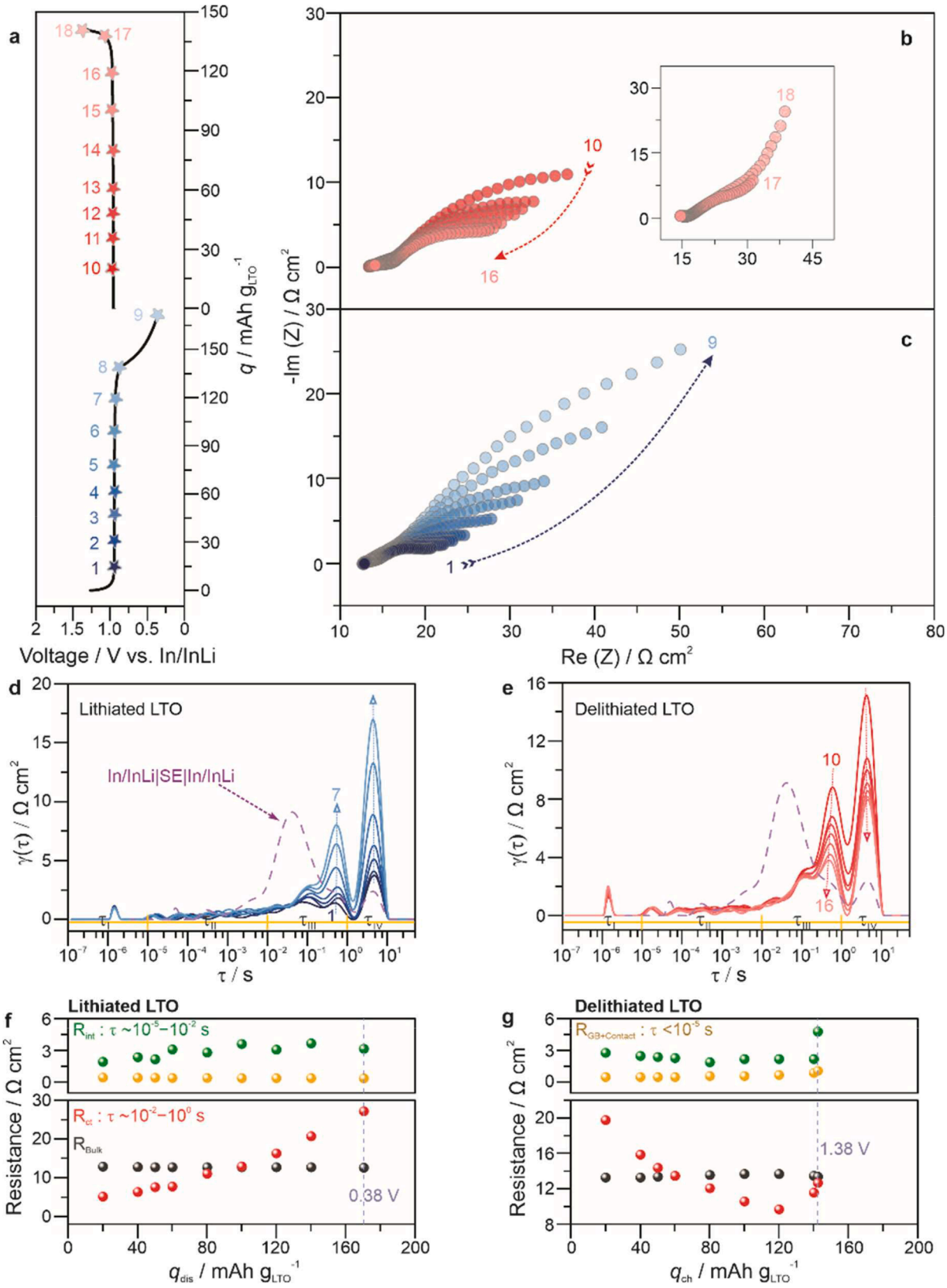

Fig. 3. *In situ* EIS-DRT analysis of the In/InLi|SE|LTO cell. (a) Voltage profile with selected SOCs labeled from 1 to 18. (b, c) Corresponding Nyquist plots and (d, e) DRT patterns during discharge and charge. Specific time constant regimes are indicated. (f, g) Fitted resistances (SE bulk, SE GB together with the contact resistance, interphase, and charge transfer) are categorized according to their characteristic time constants.

lithiation of LTO, from SOC 1 to 9, R_{int} shows a subtle and fluctuating increase, whereas R_{ct} undergoes substantial growth (from 5.1 to 27.2 Ω cm^2). Conversely, in the subsequent delithiation process, both R_{int} and R_{ct} exhibit V-shaped changes. Importantly, during the major interfacial processes, R_{ct} follows a declining trend in the plateau region (SOC 10 to 16) before increasing again with progressing transition toward the spinel phase (SOC 16 to 18).

As evident from **Table S4**, the continuous delithiation of LTO during charge leads to a similar trend in potential drift to that observed during OCV monitoring. Given the limited specific capacity for prelithiation (50 mAh g_{LTO}^{-1}), the observed potential drift agrees well with the changes in capacity and OCV seen for SOC 14 to 17, involving a steady increase (from selected points in time 1 to 5, corresponding to SOC 14 to 16) and then an accelerated increase (from selected points in time 5 to 7, corresponding to SOC 16 to 17). Interestingly, the continuous increase in R_{ct} from the selected points in times 1 to 5 contrasts with the change in R_{ct} from SOC 14 to 16 during delithiation. This suggests that microstructural degradation of the LTO electrode contributes more significantly to the increase in charge-transfer resistance than changes in SOC during the period of steady potential drift. Within the accelerated regime, the change from SOC 16 to 17 results in a substantial increase in potential, mirroring the trend observed for the selected points in time 6 to 7. Additional charge-transfer resistance due to transitioning to the final spinel phase further contributes to the overall increase in R_{ct}.

In brief, focusing on the potential drift in the In/InLi|SE|LTO 2E cell, we revisited the kinetics of LTO in SSBs. Specifically, we conducted a comprehensive evaluation of the stability of the proposed LTO-RE considering the potential drift and behavior of the electrode. Notably, under conditions of resting, low currents, or minimal cell utilization, the In/InLi electrode remains stable and largely unaffected, as evidenced by OCV monitoring and *in situ* EIS measurements. However, prolonged cycling leads to changes in microstructure and increases in interfacial resistance [17].

The EIS-DRT analysis of the 2E cell provides important insights into the individual kinetic processes of the electrodes, identified by characteristic time constants. However, overlapping impedances/time constants from coupled electrodes pose challenges in objectively evaluating their (individual) contributions to interfacial degradation, particularly in regimes dominated by charge-transfer processes. Consequently, we explored the feasibility of decoupling in the designed 3E cell. The analysis emphasizes the value and ultimately the necessity of the 3E approach.

2.4. Comparison between In/InLi|SE|LTO-RE|SE|LTO 3E and In/InLi|SE|LTO 2E cells

As depicted in Fig. 4**a**, following a 1 h resting period post assembly, the In/InLi|SE|LTO-RE|SE|LTO 3E cell allowed successful deconvolution of potentials of the two individual electrodes. The black, blue, and red curves represent the cell voltage (WE/CE), the WE/RE potential (LTO vs. LTO-RE), and the CE/RE potential (In/InLi vs. LTO-RE), respectively. Because the In/InLi CE has a stable potential of 0.622 V vs. Li^+/Li under OCV conditions, the initial (reference) potential of the LTO-RE was indirectly determined to be 0.955 V vs. In/InLi, corresponding to 1.577 V vs. Li^+/Li.

During the formation cycle at 0.1C in a voltage window of 0.38–1.38 V vs. In/InLi (equivalent to about 1.0–2.0 V vs. Li^+/Li), as shown in Fig. 4**b** and **c**, LTO delivered virtually identical capacities to the 2E counterpart, with q_{ch} approaching 139 mAh g_{LTO}^{-1} (see Fig. 4**c**). Fig. 4**d** and **e** present the individual potentials of the LTO and In/InLi electrodes during discharge and charge, respectively. The overpotential of In/InLi was derived from the difference between the measured CE/RE potential and that determined under OCV conditions, with a constant reference potential in absolute terms. The average overpotential was found to be slightly higher during discharge/delithiation (5 mV) compared to charge/lithiation (2 mV), corroborating findings from coulometric titration tests reported in the literature [13].

2.5. Validation of 3E impedance measurements

The evaluation of the 3E cell setup demonstrates highly reliable performance (similar to that of the 2E counterpart) in terms of capacities and individual potentials. The critical functionality in deconvoluting the impedances of individual electrodes was further validated. From the analysis of the In/InLi|SE|LTO 2E cell, it is apparent that LTO exhibits a SOC-dependent impedance response, as illustrated in Fig. 3. In the proposed combination of LTO and In/InLi, major interface-related charge-transfer processes were observed in the time constant region of

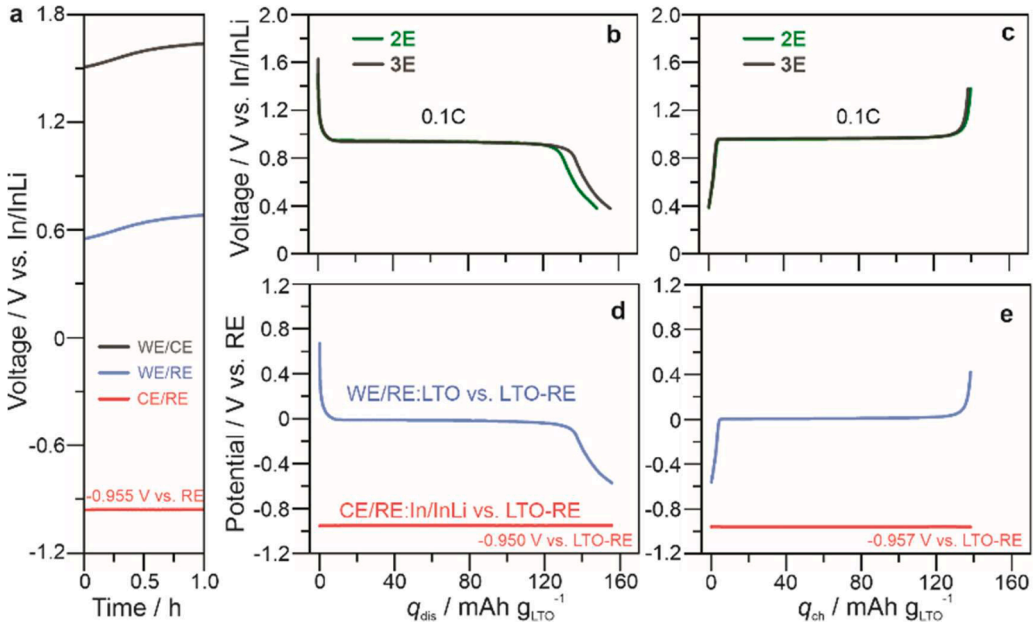

Fig. 4. Comparision of electrochemical performance between In/InLi|SE|LTO-RE|SE|LTO and In/InLi|SE|LTO cells. (a) Potential tracking of WE/RE, WE/CE, and CE/RE during initial OCV resting. (b, c) Voltage profiles of 2E and 3E cells at 0.1C during (b) discharge and (c) charge. (d, e) Potential tracking of WE/RE and CE/RE during (d) discharge and (e) charge.

τ_{III} (10^{-2}–10^{0} s), revealing severe overlap between the electrodes. Therefore, impedance measurements performed using 2E cell setups cannot accurately differentiate between the contributions of the individual electrodes, potentially leading to misinterpretations.

Following the electrochemical testing, the impedance of the 3E cell was measured at the end of charge, corresponding to the delithiated state of LTO and lithiated state of In/InLi. Three independent measurements were conducted to gather data from the WE/RE, the CE/RE, and the WE/CE, as shown in Fig. 5**a**. The LTO WE exhibits a semicircle in the medium-frequency range, followed by a Warburg-like capacitive tail, indicative of the diffusive processes occurring in the fully delithiated LTO particles. In contrast, the In/InLi CE displays only depressed semicircles below 1.5 kHz, mainly attributed to the charge-transfer process between the In/InLi and the SE. The sum of the WE and CE impedances closely matches with the 2E results, except for some deviations in the high-frequency region (above 100 kHz).

To further verify and evaluate the discrepancies between the 2E and 3E data, a residuals analysis proposed by Hertle *et al.* was performed [16]. Figs. 5**b** and **c** indicate that the real and imaginary parts exhibit residuals within 1.5 and 10% below 100 kHz. It is worth noting that impedance measurements at high frequencies are more vulnerable to the device and circuitry, cell preparation, and testing conditions. Deviations and artifacts in the high-frequency range commonly arise from the connection cables, current collectors, and/or mechanical contact issues. Improvements could be made by (i) ensuring a more stable environment during the measurement, (ii) limiting cell transportation between different cyclers, and (iii) optimizing the connection between the electrodes and the measurement device. However, the significant overlap of the 3E and 2E data from 100 kHz through the medium- to low-frequency range with low residuals demonstrates the high reliability of resolving individual impedances. The "stable" frequency range is sufficient to cover the interface kinetics of most energy-storage materials [23]. The validity of the gathered impedance data was further confirmed by a Kramers-Kronig (K-K) test, as detailed in **Figure S8** and discussed in **Supplementary Note 4**.

2.6. *Interface kinetics of LTO and In/InLi from 3E EIS-DRT analysis*

Fig. 6**a** illustrates the individual DRT patterns for LTO and In/InLi. Surprisingly, the kinetic processes identified by the distinct peaks show significant overlap across the different timescales, with notable variations in peak position and intensity. The primary interfacial contribution, located in the τ_{III} regime, is associated with charge-transfer processes for both LTO and In/InLi. The most sluggish kinetic process, observed in the τ_{IV} regime of LTO, is attributed to diffusive polarization, which is the rate-limiting step in the 3E cell performance. In contrast, lithiated In/InLi exhibits more favorable lithium diffusivity compared to the fully delithiated LTO, as evidenced by the stark contrast in peak

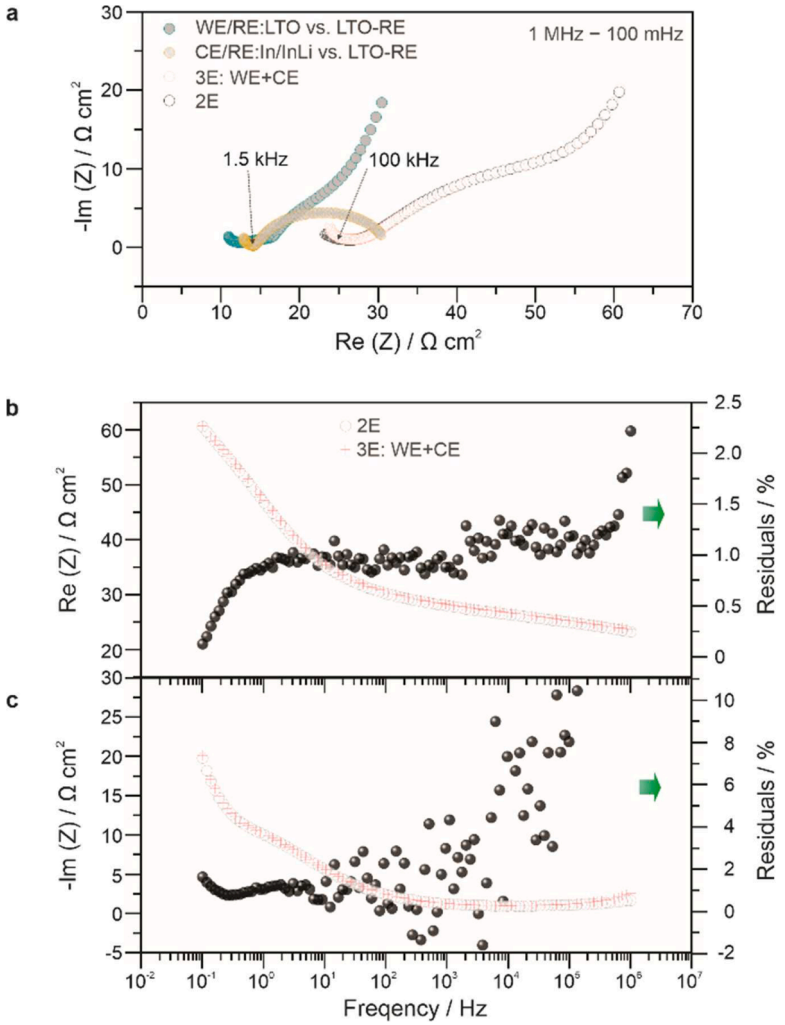

Fig. 5. 3E impedance measurement of the In/InLi|SE|LTO-RE|SE|LTO cell. (a) Nyquist plots for the individual electrodes, with a comparison of overlap between the 2E (WE/CE) and 3E (WE+CE) data. (b, c) Comparisons of impedance results for the real and imaginary parts between the 2E and combined 3E data. Hollow circles represent the 2E results, red crosses the 3E results, and solid circles show the residuals.

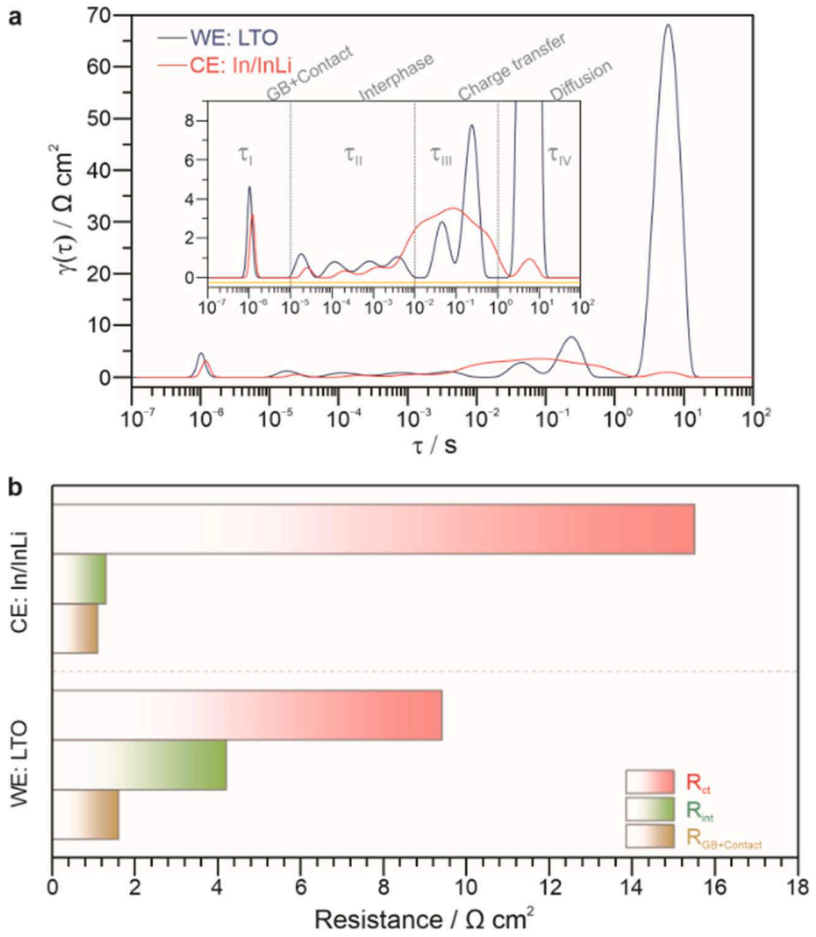

Fig. 6. 3E EIS-DRT analysis of individual electrodes (WE:LTO/CE:In/InLi). (a) DRT patterns. The inset is a zoomed-in view showing peaks reflecting the involved kinetic processes. (b) Fitted resistances (SE GB together with the contact resistance, interphase, and charge transfer) are categorized according to their characteristic time constants.

intensities within the τ_{IV} regime.

Regarding the analysis of interface kinetics, it becomes clear that neither ECM fitting in the frequency domain nor DRT analysis in the time domain can objectively evaluate the contributions of the involved processes for both electrodes in a 2E system due to overlapping timescales. Furthermore, the traditional separation of frequency ranges, specifically the medium- and low-frequency range, needs to be redefined. Assignments should focus on attributing contributions to charge transport across the as-formed interphases [cathode electrolyte interphase (CEI) or solid electrolyte interphase (SEI)] and ionic charge transfer between the active electrode material and the SE, respectively, rather than simply categorizing them by cathode and anode.

Quantitatively, the $R_{GB+Contact}$ is similar for both the LTO and In/InLi electrodes, as shown in Fig. 6**b**. The R_{int} of In/InLi (1.3 Ω cm^2) is notably lower than that of LTO (4.2 Ω cm^2), yet both with low values suggesting favorable charge transport through the as-formed interphases. The R_{ct}, which is pronounced in the τ_{III} regime, is higher for In/InLi (15.5 Ω cm^2) compared to LTO (9.4 Ω cm^2), despite the lithiated state of In/InLi, which typically facilitates fast charge transfer. This indicates that charge transfer at the In/InLi|SE interface can be adversely affected, especially after prolonged testing. The DRT peak fits and a summary of the fitted parameters are provided in **Figure S9** and **Tables S10** and **S11**.

Unlike the quasi zero-strain behavior of LTO, In/InLi experiences severe volume changes that lead to microstructural degradation and direcly affect the pathways for ion and electron transport, resulting in inferior kinetics over time. A suggested improvement in the preparation of In/InLi electrodes by mixing with the SE could facilitate the kinetics of the InLi alloy phase near the interface [15]. Further 3E-assisted investigations exploring the evolution of different materials during extended cycling will be detailed in subsequent studies.

3. Conclusions

In the present work, we report on a novel strategy for preparing 3E SSB cells by utilizing a LTO-containing composite as RE. A systematic investigation into the potential/SOC/kinetics relationship of LTO was conducted by EIS-DRT analysis to thoroughly evaluate the as-prepared RE. The proposed LTO-RE provides a stable reference potential with minimal drift and low growth rate in charge-transfer resistance (by about 0.003 Ω cm^2 h^{-1}), offering optimal conditions for practical long-term testing in 3E SSBs, as well as to collect high-quality data for deconvoluting impedance components. Significant overlap across the full timescales of the LTO and In/InLi electrodes is revealed. DRT analysis clearly indicates the challenges of identifying contributions from individual electrodes when examined either in the frequency or time domain using 2E cells. The electrochemically prelithiated LTO composite extends the applicability of the 3E setup to other promising SSB systems while avoiding SE heterogeneities between the RE and the separator layer. LTO, used as active material in the RE, is particularly favorable, facilitating stable performance in low-temperature 3E testing scenarios. We believe that the setup presented herein helps bridge the performance gap between 2E and 3E configurations, providing insights into key issues in SSB research and development.

4. Experimental section

Materials. Argyrodite Li_6PS_5Cl (NEI Corp.) as SE was used as received. Super C65 carbon additive (TIMCAL Ltd.) and carbon-coated LTO (NEI Corp.) were dried at 300 °C under dynamic vacuum overnight prior to use. For the 2E and 3E SSB testing, In foil (Changsha Santech Materials Co., Ltd.) of 100 or 125 μm thickness was punched into discs of 9 mm diameter. Li foil (Albemarle Germany GmbH) of 50 μm thickness was punched into discs of 6 mm diameter. SS wire (Thermo Scientific) of 127 μm diameter served as current collector in the 3E cell preparation.

Composite preparation and 2E cell assembly. The LTO composite was prepared in an 80 mL zirconia milling jar containing the carbon-coated LTO, SE, and Super C65 in a weight ratio of 30:65:5, along with 10 zirconia balls of diameter 10 mm. After sealing in an argon glovebox [$p(H_2O)/p < 0.1$ ppm and $p(O_2)/p < 0.1$ ppm], the composite was milled at 140 rpm for 30 min using a FRITSCH planetary mill. 2E cells, In/InLi|SE|LTO, were assembled using two SS dies as current collectors and a PEEK ring of inner diameter 10 mm. Initially, 100 mg of SE was spread into the PEEK ring and densified at 62.5 MPa. Then, around 20 or 25 mg of LTO composite was placed on one side of the SE separator layer and densified at 440 MPa for 3 min. On the opposite side (without additional pressing), the In/InLi alloy served as CE, with the In foil facing the SE.

Prelithiation of LTO. To prepare the RE for application in 3E cells, carbon-coated LTO as active material was first prelithiated in a 2E cell. The latter cell was assembled as described above, with the potential range set between 0.38 and 1.38 V vs. In/InLi, equivalent to about 1.0–2.0 V vs. Li^+/Li. The optimized protocol involved two formation cycles at 0.1C (1C = 175 mA g_{LTO}^{-1}), followed by discharge with a specific capacity limitation of 50 mAh g_{LTO}^{-1}. After prelithiation, the cell was disassembled, and the pellet stack was harvested in an argon glovebox. The prelithiated LTO composite electrode can be readily broken into pieces and then used as RE in the assembly of 3E cells. The attached SE separator layer was carefully scraped off using sandpaper.

3E cell assembly. The cell setup mirrored the 2E architecture but included two symmetrical holes in the PEEK ring for the SS wire. One of the aforementioned pieces was placed on the SS wire, followed by the addition of 80 mg of SE and densification at 125 MPa. This process was repeated for the second piece, ensuring overlap. A total of 160 mg of SE and the embedded two pieces (fragments) of prelithiated LTO composite completed the RE assembly. The final 3E cell configuration used 20 mg of LTO composite as WE and In/InLi alloy as CE to compare the performance to the 2E counterpart. Both the 2E and 3E cells were sealed into a pouch for electrochemical testing.

Electrochemical testing. The cells were examined at 45 °C and under an external pressure of 81 MPa. Testing was carried out using either a MACCOR battery cycler or a Bio-Logic SP-300 multichannel potentiostat. EIS measurements for both the 2E and 3E configurations were performed across a frequency range from 1 MHz to 100 mHz, with the voltage amplitude set at 7 mV. For the In/InLi|SE|LTO cells with 25 mg LTO composite loading, *in situ* EIS measurements were conducted at selected SOCs, as outlined in **Table S4**. To ensure thermodynamic equilibrium, a rest period of at least 15 min was implemented prior to each measurement. The 3E impedance was analyzed at the end of charge, corresponding to the completion of LTO delithiation and lithiation of In/InLi. Impedance measurements on individual electrodes, including WE:LTO, CE:In/InLi, and WE/CE (2E configuration), were conducted separately, with each being allowed a rest period of 15 min. DRT analysis was performed using RelaxIS software (rhd instruments). Complex data were used to conduct the DRT transformation with Gaussian radial basis function (RBF)-based discretization. The second derivative of the distribution function was used as the penalty item with a shape factor value of 0.5 and regularization parameter $\lambda = 10^{-5}$ for all patterns in this work. By applying multiple Gaussian peak functions, DRT patterns with multiple peaks were fitted to determine the characteristic time constants and peak areas. More details are provided in the **Supplementary Note 2**. The K-K test was performed using the Lin-KK tool (https://www.iam.kit.edu/et/english/Lin-KK.php) [55,56].

Physical characterization. SEM imaging was performed using a Leo 1530 microscope (Zeiss) at an accelerating voltage of 10 kV. EDS utilized an Oxford X-MaxN detector at 20 kV. Cross-sectional polishing of pellets was performed using a JEOL IB-19510CP polisher with an Ar-gas source. Powder XRD patterns were recorded on a STOE Stadi-P diffractometer with a Mo anode ($\lambda = 0.70926$ Å) and analyzed using GSAS-II for Rietveld refinement [57].

Declaration of generative AI and AI-assisted technologies in the writing process

During the preparation of this work, the author(s) used ChatGPT4.0 (by OpenAI) to polish the writing to improve upon language and readability. The author(s) reviewed and edited the content as needed and take full responsibility for the content of the published article.

CRediT authorship contribution statement

Ruizhuo Zhang: Writing – original draft, Visualization, Validation, Software, Investigation, Formal analysis, Conceptualization. **Aleksandr Kondrakov:** Writing – review & editing, Supervision, Project administration, Funding acquisition. **Jürgen Janek:** Writing – review & editing, Supervision, Funding acquisition. **Torsten Brezesinski:** Writing – review & editing, Supervision, Project administration, Funding acquisition.

Declaration of competing interest

The authors declare that they have no known competing financial interests or personal relationships that could have appeared to influence the work reported in this paper.

Acknowledgements

This study was supported by BASF SE. The authors acknowledge the support from the Karlsruhe Nano Micro Facility (KNMFi, www.knmf.kit.edu), a Helmholtz research infrastructure at Karlsruhe Institute of Technology (KIT, www.kit.edu). Special thanks to Michael Hesselschwerdt from the mechanical workshop for his assistance in fabricating the 3E cell used in this study.

Supplementary materials

Supplementary material associated with this article can be found, in the online version, at doi:10.1016/j.ensm.2025.104000.

Data availability

Data will be made available on request.

References

[1] Porsche Consulting, The race for solid-state batteries. https://magazine.porsche-consulting.com/en/the-race-for-solid-state-batteries/, 2023 (accessed 8 November 2024).
[2] J. Janek, W.G. Zeier, A solid future for battery development, Nat. Energy 1 (2016) 16141.
[3] D. Ren, L. Lu, R. Hua, G. Zhu, X. Liu, Y. Mao, X. Rui, S. Wang, B. Zhao, H. Cui, M. Yang, H. Shen, C.-Z. Zhao, L. Wang, X. He, S. Liu, Y. Hou, T. Tan, P. Wang, Y. Nitta, M. Ouyang, Challenges and opportunities of practical sulfide-based all-solid-state batteries, eTransportation 18 (2023) 100272.
[4] J. Du, J. Lin, R. Zhang, S. Wang, S. Indris, H. Ehrenberg, A. Kondrakov, T. Brezesinski, F. Strauss, Electrochemical testing and benchmarking of compositionally complex lithium argyrodite electrolytes for all-solid-state battery application, Batter. Supercaps 7 (2024) e202400112.

[5] Y. Li, S. Song, H. Kim, K. Nomoto, H. Kim, X. Sun, S. Hori, K. Suzuki, N. Matsui, M. Hirayama, T. Mizoguchi, T. Saito, T. Kamiyama, R. Kanno, A lithium superionic conductor for millimeter-thick battery electrode, Science 381 (2023) 50–53.

[6] L. Ye, X. Li, A dynamic stability design strategy for lithium metal solid state batteries, Nature 593 (2021) 218–222.

[7] Y. Zhu, X. He, Y. Mo, Origin of outstanding stability in the lithium solid electrolyte materials: insights from thermodynamic analyses based on first-principles calculations, ACS Appl. Mater. Interfaces 7 (2015) 23685–23693.

[8] A. Banerjee, X. Wang, C. Fang, E.A. Wu, Y.S. Meng, Interfaces and interphases in all-solid-state batteries with inorganic solid electrolytes, Chem. Rev. 120 (2020) 6878–6933.

[9] R. Zhang, Y. Ma, Y. Tang, D. Goonetilleke, T. Diemant, J. Janek, A. Kondrakov, T. Brezesinski, Conformal Li_2HfO_3/HfO_2 nanoparticle coatings on layered Ni-rich oxide cathodes for stabilizing interfaces in all-solid-state batteries, Chem. Mater. 35 (2023) 6835–6844.

[10] A. Morchhale, Z. Tang, C. Yu, R. Farahati, J.-H. Kim, Coating materials and processes for cathodes in sulfide-based all solid-state batteries, Curr. Opin. Electrochem. 39 (2023) 101251.

[11] A.M. Nolan, Y. Liu, Y. Mo, Solid-state chemistries stable with high-energy cathodes for lithium-ion batteries, ACS Energy Lett 4 (2019) 2444–2451.

[12] S.H. Jung, K. Oh, Y.J. Nam, D.Y. Oh, P. Brüner, K. Kang, Y.S. Jung, Li_3BO_3–Li_2CO_3: rationally designed buffering phase for sulfide all-solid-state Li-ion batteries, Chem. Mater. 30 (2018) 8190–8200.

[13] A.L. Santhosha, L. Medenbach, J.R. Buchheim, P. Adelhelm, The indium− lithium electrode in solid-state lithium-ion batteries: phase formation, redox potentials, and interface stability, Batter. Supercaps 2 (2019) 524–529.

[14] S. Puls, E. Nazmutdinova, F. Kalyk, H.M. Woolley, J.F. Thomsen, Z. Cheng, A. Fauchier-Magnan, A. Gautam, M. Gockeln, S.-Y. Ham, M.T. Hasan, M.-G. Jeong, D. Hiraoka, J.S. Kim, T. Kutsch, B. Lelotte, P. Minnmann, V. Miß, K. Motohashi, D. L. Nelson, F. Ooms, F. Piccolo, C. Plank, M. Rosner, S.E. Sandoval, E. Schlautmann, R. Schuster, D. Spencer-Jolly, Y. Sun, B.S. Vishnugopi, R. Zhang, H. Zheng, P. Adelhelm, T. Brezesinski, P.G. Bruce, M. Danzer, M. El Kazzi, H. Gasteiger, K. B. Hatzell, A. Hayashi, F. Hippauf, J. Janek, Y.S. Jung, M.T. McDowell, Y.S. Meng, P.P. Mukherjee, S. Ohno, B. Roling, A. Sakuda, J. Schwenzel, X. Sun, C. Villevieille, M. Wagemaker, W.G. Zeier, N.M. Vargas-Barbosa, Benchmarking the reproducibility of all-solid-state battery cell performance, Nat. Energy 9 (2024) 1310–1320.

[15] S. Yanev, C. Heubner, K. Nikolowski, M. Partsch, H. Auer, A. Michaelis, Editors' choice—Alleviating the kinetic limitations of the Li-In alloy anode in all-solid-state batteries, J. Electrochem. Soc. 171 (2024) 020512.

[16] J. Hertle, F. Walther, B. Mogwitz, S. Schröder, X. Wu, F.H. Richter, J. Janek, Miniaturization of reference electrodes for solid-state lithium-ion batteries, J. Electrochem. Soc. 170 (2023) 040519.

[17] J. Aspinall, Y. Chart, H. Guo, P. Shrestha, M. Burton, M. Pasta, Effect of microstructure on the cycling behavior of Li–In alloy anodes for solid-state batteries, ACS Energy Lett 9 (2024) 578–585.

[18] S. Luo, Z. Wang, X. Li, X. Liu, H. Wang, W. Ma, L. Zhang, L. Zhu, X. Zhang, Growth of lithium-indium dendrites in all-solid-state lithium-based batteries with sulfide electrolytes, Nat. Commun. 12 (2021) 6968.

[19] F. Walther, F. Strauss, X. Wu, B. Mogwitz, J. Hertle, J. Sann, M. Rohnke, T. Brezesinski, J. Janek, The working principle of a $Li_2CO_3/LiNbO_3$ coating on NCM for thiophosphate-based all-solid-state batteries, Chem. Mater. 33 (2021) 2110–2125.

[20] F. Walther, R. Koerver, T. Fuchs, S. Ohno, J. Sann, M. Rohnke, W.G. Zeier, J. Janek, Visualization of the interfacial decomposition of composite cathodes in argyrodite-based all-solid-state batteries using time-of-flight secondary-ion mass spectrometry, Chem. Mater. 31 (2019) 3745–3755.

[21] R. Zhang, F. Strauss, L. Jiang, L. Casalena, L. Li, J. Janek, A. Kondrakov, T. Brezesinski, Transition-metal interdiffusion and solid electrolyte poisoning in all-solid-state batteries revealed by cryo-TEM, Chem. Commun. 59 (2023) 4600–4603.

[22] S. Kobayashi, H. Watanabe, T. Kato, F. Mizuno, A. Kuwabara, Atomic-scale observations of oxygen release degradation in sulfide-based all-solid-state batteries with layered oxide cathodes, ACS Appl. Mater. Interfaces 14 (2022) 39459–39466.

[23] Y. Lu, C.-Z. Zhao, J.-Q. Huang, Q. Zhang, The timescale identification decoupling complicated kinetic processes in lithium batteries, Joule 6 (2022) 1172–1198.

[24] R. Soni, J.B. Robinson, P.R. Shearing, D.J.L. Brett, A.J.E. Rettie, T.S. Miller, Lithium-sulfur battery diagnostics through distribution of relaxation times analysis, Energy Storage Mater 51 (2022) 97–107.

[25] J. Chen, E. Quattrocchi, F. Ciucci, Y. Chen, Charging processes in lithium-oxygen batteries unraveled through the lens of the distribution of relaxation times, Chem 9 (2023) 2267–2281.

[26] P. Lu, Y. Wu, D. Wu, F. Song, T. Ma, W. Yan, X. Zhu, F. Guo, J. Lu, J. Peng, L. Chen, H. Li, F. Wu, Rate-limiting mechanism of all-solid-state battery unravelled by low-temperature test-analysis flow, Energy Storage Mater 67 (2024) 103316.

[27] J.K. Eckhardt, P.J. Klar, J. Janek, C. Heiliger, Interplay of dynamic constriction and interface morphology between reversible metal anode and solid electrolyte in solid state batteries, ACS Appl. Mater. Interfaces 14 (2022) 35545–35554.

[28] J.K. Eckhardt, T. Fuchs, S. Burkhardt, P.J. Klar, J. Janek, C. Heiliger, Guidelines for impedance analysis of parent metal anodes in solid-state batteries and the role of current constriction at interface voids, heterogeneities, and SEI, Adv. Mater. Interfaces 10 (2023) 2202354.

[29] F.J. Simon, L. Blume, M. Hanauer, U. Sauter, J. Janek, Development of a wire reference electrode for lithium all-solid-state batteries with polymer electrolyte: FEM simulation and experiment, J. Electrochem. Soc. 165 (2018) A1363–A1371.

[30] L. Xu, Y. Xiao, Z.X. Yu, Y. Yang, C. Yan, J.Q. Huang, Revisiting the electrochemical impedance spectroscopy of porous electrodes in Li-ion batteries by employing reference electrode, Angew. Chem. Int. Ed. 63 (2024) e202406054.

[31] P. Stehle, D. Rutz, A.M. Bazzoun, C. Seidl, I. Bauer, M. Anjass, Application of perforated reference electrodes in small cell formats for rate tests and electrochemical impedance spectroscopy, Energy Technol 11 (2023) 2300278.

[32] N. Qin, L. Jin, G. Xing, Q. Wu, J. Zheng, C. Zhang, Z. Chen, J.P. Zheng, Decoupling accurate electrochemical behaviors for high-capacity electrodes via reviving three-electrode vehicles, Adv. Energy Mater. 13 (2023) 2204077.

[33] L.M. Riegger, S. Mittelsdorf, T. Fuchs, R. Rueß, F.H. Richter, J. Janek, Evolution of the interphase between argyrodite-based solid electrolytes and the lithium metal anode—the kinetics of solid electrolyte interphase growth, Chem. Mater. 35 (2023) 5091–5099.

[34] G. Fukunishi, A. Ikezawa, T. Okajima, F. Kitamura, K. Suzuki, M. Hirayama, R. Kanno, H. Arai, Impedance analysis and cyclability evaluation of graphite composite electrodes with all-solid-state three-electrode cells, ACS Appl. Energy Mater. 6 (2023) 10908–10917.

[35] T. Koç, M. Hallot, E. Quemin, B. Hennequart, R. Dugas, A.M. Abakumov, C. Lethien, J.-M. Tarascon, Toward optimization of the chemical/electrochemical compatibility of halide solid electrolytes in all-solid-state batteries, ACS Energy Lett 7 (2022) 2979–2987.

[36] Y.J. Nam, K.H. Park, D.Y. Oh, W.H. An, Y.S. Jung, Diagnosis of failure modes for all-solid-state Li-ion batteries enabled by three-electrode cells, J. Mater. Chem. A 6 (2018) 14867–14875.

[37] R. Dugas, Y. Dupraz, E. Quemin, T. Koç, J.-M. Tarascon, Engineered three-electrode cells for improving solid state batteries, J. Electrochem. Soc. 168 (2021) 090508.

[38] A. Ikezawa, G. Fukunishi, T. Okajima, F. Kitamura, K. Suzuki, M. Hirayama, R. Kanno, H. Arai, Performance of $Li_4Ti_5O_{12}$-based reference electrode for the electrochemical analysis of all-solid-state lithium-ion batteries, Electrochem. Commun. 116 (2020) 106743.

[39] C. Sedlmeier, R. Schuster, C. Schramm, H.A. Gasteiger, A micro-reference electrode for electrode-resolved impedance and potential measurements in all-solid-state battery pouch cells and its application to the study of indium-lithium anodes, J. Electrochem. Soc. 170 (2023) 030536.

[40] D. Rutz, F. Brauchle, P. Stehle, I. Bauer, T. Jacob, An experimental method to determine the measurement error of reference electrodes within lithium-ion batteries, ChemElectroChem 10 (2023) e202300216.

[41] A.-T. Tran, F. Huet, K. Ngo, P. Rousseau, Artefacts in electrochemical impedance measurement in electrolytic solutions due to the reference electrode, Electrochim. Acta. 56 (2011) 8034–8039.

[42] L.H.J. Raijmakers, M.J.G. Lammers, P.H.L. Notten, A new method to compensate impedance artefacts for Li-ion batteries with integrated micro-reference electrodes, Electrochim. Acta. 259 (2018) 517–533.

[43] M. Ender, J. Illig, E. Ivers-Tiffée, Three-electrode setups for lithium-ion batteries, J. Electrochem. Soc. 164 (2017) A71–A79.

[44] J.K. Eckhardt, S. Kremer, L. Merola, J. Janek, Heteroionic interfaces in hybrid solid-state batteries—current constriction at the interface between different solid electrolytes, ACS Appl. Mater. Interfaces 16 (2024) 18222–18235.

[45] Q. Zhou, X. Yang, X. Xiong, Q. Zhang, B. Peng, Y. Chen, Z. Wang, L. Fu, Y. Wu, A solid electrolyte based on electrochemical active $Li_4Ti_5O_{12}$ with PVDF for solid state lithium metal battery, Adv. Energy Mater. 12 (2022) 2201991.

[46] P. Zou, C. Wang, Y. He, H.L. Xin, Broadening solid ionic conductor selection for sustainable and earth-abundant solid-state lithium metal batteries, Energy Environ. Sci. 16 (2023) 5871–5880.

[47] M. Wagemaker, D.R. Simon, E.M. Kelder, J. Schoonman, C. Ringpfeil, U. Haake, D. Lützenkirchen-Hecht, R. Frahm, F.M. Mulder, A kinetic two-phase and equilibrium solid solution in spinel $Li_{4+x}Ti_5O_{12}$, Adv. Mater. 18 (2006) 3169–3173.

[48] M. Wagemaker, E.R.H. van Eck, A.P.M. Kentgens, F.M. Mulder, Li-ion diffusion in the equilibrium nanomorphology of spinel $Li_{4+x}Ti_5O_{12}$, J. Phys. Chem. B. 113 (2009) 224–230.

[49] M. Kitta, T. Akita, Y. Maeda, M. Kohyama, Study of surface reaction of spinel $Li_4Ti_5O_{12}$ during the first lithium insertion and extraction processes using atomic force microscopy and analytical transmission electron microscopy, Langmuir 28 (2012) 12384–12392.

[50] Y. Lu, C.-Z. Zhao, R. Zhang, H. Yuan, L.-P. Hou, Z.-H. Fu, X. Chen, J.-Q. Huang, Q. Zhang, The carrier transition from Li atoms to Li vacancies in solid-state lithium alloy anodes, Sci. Adv. 7 (2021) eabi5520.

[51] R. Dedryvère, D. Foix, S. Franger, S. Patoux, L. Daniel, D. Gonbeau, Electrode/electrolyte interface reactivity in high-voltage spinel $LiMn_{1.6}Ni_{0.4}O_4/Li_4Ti_5O_{12}$ lithium-ion battery, J. Phys. Chem. C 114 (2010) 10999–11008.

[52] K. Wu, J. Yang, X.-Y. Qiu, J.-M. Xu, Q.-Q. Zhang, J. Jin, Q.-C. Zhuang, Study of spinel $Li_4Ti_5O_{12}$ electrode reaction mechanism by electrochemical impedance spectroscopy, Electrochim. Acta. 108 (2013) 841–851.

[53] N. Takami, K. Hoshina, H. Inagaki, Lithium diffusion in $Li_{4/3}Ti_{5/3}O_4$ particles during insertion and extraction, J. Electrochem. Soc. 158 (2011) A725–A730.

[54] E. Quemin, R. Dugas, A. Chaupatnaik, G. Rousse, R. Chometon, B. Hennequart, J.-M. Tarascon, An advanced cell for measuring in situ electronic conductivity evolutions in all-solid-state battery composites, Adv. Energy Mater. 13 (2023) 2301105.

[55] B.A. Boukamp, A linear Kronig-Kramers transform test for immittance data validation, J. Electrochem. Soc. 142 (1995) 1885–1894.

[56] M. Schönleber, D. Klotz, E. Ivers-Tiffée, A method for improving the robustness of linear Kramers-Kronig validity tests, Electrochim. Acta. 131 (2014) 20–27.

[57] B.H. Toby, R.B. Von Dreele, GSAS-II: the genesis of a modern open-source all purpose crystallography software package, J. Appl. Crystallogr. 46 (2013) 544–549.